Journal of Power Sources 226 (2013) 241–248

Contents lists available at SciVerse ScienceDirect

Journal of Power Sources

journal homepage: www.elsevier.com/locate/jpowsour

High-performance Sn@carbon nanocomposite anode for lithium batteries

Ida Meschini [a], Francesco Nobili [b], Marilena Mancini [b], Roberto Marassi [b], Roberto Tossici [b], Alberto Savoini [c], Maria Letizia Focarete [d], Fausto Croce [a,*]

[a] Dipartimento di Scienze del Farmaco, Università "G. d'Annunzio" Chieti-Pescara, Via dei Vestini 31, Chieti 66100, Italy
[b] Scuola di Scienze e Tecnologie, Sezione Chimica, Università degli Studi di Camerino, Via S. Agostino 1, Camerino 62032, MC, Italy
[c] Istituto ENI Donegani, Via Fauser 4, Novara 28100, Italy
[d] Dipartimento di Chimica "G. Ciamician" e Consorzio Interuniversitario Nazionale per la Scienza e Tecnologia dei Materiali (INSTM, UdR Bologna), Università di Bologna , Via Selmi 2, 40126 Bologna, Italy

HIGHLIGHTS

- A Sn/C anode material is prepared by co-electrospinning and heat treatment in Ar/H_2.
- The morphology exhibits nanosized Sn embedded in multichannel carbon microtubes.
- The anode delivers outstanding capacities up to 10 C cycling rate.
- Cycle life extends to 600 cycles with stable capacity.

ARTICLE INFO

Article history:
Received 9 June 2012
Received in revised form
31 October 2012
Accepted 3 November 2012
Available online 10 November 2012

Keywords:
Li-ion battery
Sn–C anode
Electrospinning
Nanocomposite electrode

ABSTRACT

Nanosize tin particles (Sn-PMCMT) embedded in electrically conducting porous multichannel carbon microtubes are synthesized by co-electrospinning followed by air stabilization and carbonization in Ar/H_2 atmosphere. Scanning and transmission electron microscopy show that the material is nanostructured with nanosize Sn particles well embedded into the carbon host matrix.

Composite electrodes prepared using Sn-PMCMT, Super-P carbon and Na-carboxymethylcellulose as binder, exhibit a superior rate capability and exceptional cycle life in cell tests at room temperature. Discharge capacities as high as 632 mAh g^{-1} at 0.7 C rate are obtained during the first galvanostatic cycles. The delivered capacities are still in excess of 350 mAh g^{-1} after 600 cycles, most of them performed at 2 C rate. These outstanding results represent the highest performance so far reported for this type of electrode.

© 2012 Elsevier B.V. All rights reserved.

1. Introduction

Modern society thrives on massive energy utilization, but the high cost of oil, as well as the pollution of large urban areas and the CO_2-related global warming concerns, are the driving force for worldwide initiatives aimed at the utilization of alternative, renewable energy sources and at the replacement of internal combustion engines with wireless electric motors. In order to fully exploit the potentialities offered by this new paradigm of energy production and utilization, it is mandatory to be able to efficiently store and transport large quantities of energy.

In this context, batteries are electrochemical energy storage devices with the unique ability to deliver the stored chemical energy as electric energy with high conversion efficiency and without any kind of gaseous exhaust. Among all the others, Li-ion battery exceeds at least by a factor 2.5 any rivaling technology in terms of energy density (210 Wh kg^{-1} and 650 Wh l^{-1}) [1,2]. However, the use of Li-ion batteries in the emerging PHEV (plug-in hybrid electric vehicles), HEV (hybrid electric vehicles) and EV (electric vehicles) requires further improvements of parameters such as energy density, cycle life, environmental compatibility and safety.

The achievement of these demanding targets has prompted large efforts, among the global scientific community involved in lithium-ion batteries (LiBs) research, aimed at the development of innovative electrode materials having specifically engineered nanostructures [3–8]. In this context, metallic tin (Sn) has been one of the most studied candidates as anode materials for LiBs. The frantic attention devoted to this material relies on its ability of alloying 4.4 lithium atoms per Sn atom forming $Li_{4.4}Sn$, which entails the relevant theoretical capacity of about 990 mAh g^{-1}, a value greatly outperforming that of graphitic carbon

* Corresponding author. Tel.: +39 (0)871 355 4480; fax: +39 (0)871 355 4483.
E-mail address: fausto.croce@unich.it (F. Croce).

0378-7753/$ – see front matter © 2012 Elsevier B.V. All rights reserved.
http://dx.doi.org/10.1016/j.jpowsour.2012.11.004

(372 mAh g^{-1} for LiC_6) [9–11]. Nevertheless, tin anode still suffers of critical drawbacks, which hamper its practical application to LiBs. To this regard, known problems affecting metallic Sn anode operation in LiBs are the large volume expansion and contraction that occur during charging and discharging and the Sn nanoparticles coalescence during the Li-alloying process [12,13]. The former of these two phenomena results in mechanical failure and loss of electric inter-particles contact, while the latter implies a decrease of the electrochemical active surface area and a consequent increase of the actual current density, which affects the anode kinetics [14]. A common strategy to overcome these drawbacks involves a hard-confinement of nanosized Sn particles by a conducting carbon host matrix [15]. Particularly efficient to this purpose has resulted morphologies formed by Sn nanosized particles embedded into hollow carbon nanofibers prepared by electrospinning [16–19]. These composite nanostructures add up the ability to suppress the volume expansion of the Sn nanoparticles during the charge/discharge cycles with the unique property of the nanofibrillar network of favoring both the electronic and ionic charge transport during the cell operation.

In order to further improve the stability and the electrochemical performances of Li-ion anode, the optimization of the binder used in electrodes fabrication has been another common approach reported in the literature. Na-carboxymethylcellulose (Na-CMC) has been shown to be one of the more promising options, since it is a water soluble, environmentally friendly binder that acts as a surface modifier, promotes the formation of a more stable SEI [20] and improves the homogeneity and the contacts between the active material and conductive carbon particles [21].

In this work, composite, tin-containing porous multichannel carbon microtubes (Sn-PMCMT) with reticular morphology were fabricated from co-electrospun tributylphenyl-tin/polyacrylonitrile-polymethylmethacrylate (TBPT/PAN–PMMA) composite fibers by stabilization in air and carbonization in Ar/H_2 atmosphere. The resulting Sn-PMCMT was used in conjunction with Na-CMC binder as anode material for LiBs. The material exhibited a large reversible capacity and an exceptional cycling performance. To the best of our knowledge, there are only few reports on the one step fabrication of Sn nanoparticles embedded in hollow carbon nanofibers [19–22] and none utilizing TBPT as organic tin precursor. In addition, none of the reported Sn/C composite anode materials in LiBs has shown comparable performances in terms of delivered capacity, rate capability and cycle life.

2. Experimental

The precursor solution for electrospinning was prepared by dissolving 5 g of PAN (PAN, Mw = 150 kDa, Aldrich) and 5 g of PMMA (PMMA, Mw = 960 kDa, Aldrich) in 100 ml dimethylformamide (DMF, Aldrich) solvent at around 80 °C by stirring overnight. Then 12 g of tributylphenyl-tin (TBPT, Aldrich) were added to the PAN–PMMA solution under continuous stirring for at least 2 h. The resulting mixture was used as the working fluid for fabrication of PMMA–PAN–tributylphenyl-tin nanofibers by electrospinning. The working fluid was loaded into a 5 ml syringe connected by a Teflon tube to a blunt-tip stainless-steel needle. The flow rate of the solution was 20 μl min^{-1} controlled by a syringe pump (kd-Scientific, USA). The metallic needle was connected to a high voltage power supply (CZ1000R, Spellman). A voltage of 13 kV was applied between the needle and a grounded alumina foil, which was used to collect the nanofibrous mat.

The as-collected electrospun fibrous mats were stabilized in air at 250 °C for 60 min. Subsequently, the mats were carbonized in a tube furnace at 700 °C in Ar/H_2 (95 vol%/5 vol%) for 3 h to obtain the Sn particles embedded in multichannel hollow porous carbon microtubes (Sn-PMCMT). The heating rate was kept at 5 °C min^{-1}. Both the schematics and the details of synthesis procedure are reported in Fig. 1.

The morphology of pyrolyzed fibers was investigated using scanning and transmission electron microscopy (SEM, TEM) by using JEOL JSM 7600F instrumentation. EDX mapping has been acquired at K-edge of C and L-edge of Sn. The elemental composition of Sn-PMCMT was determined by chemical elemental analysis using the EA1108 CHNSO combustion elemental analyzer by Fisons.

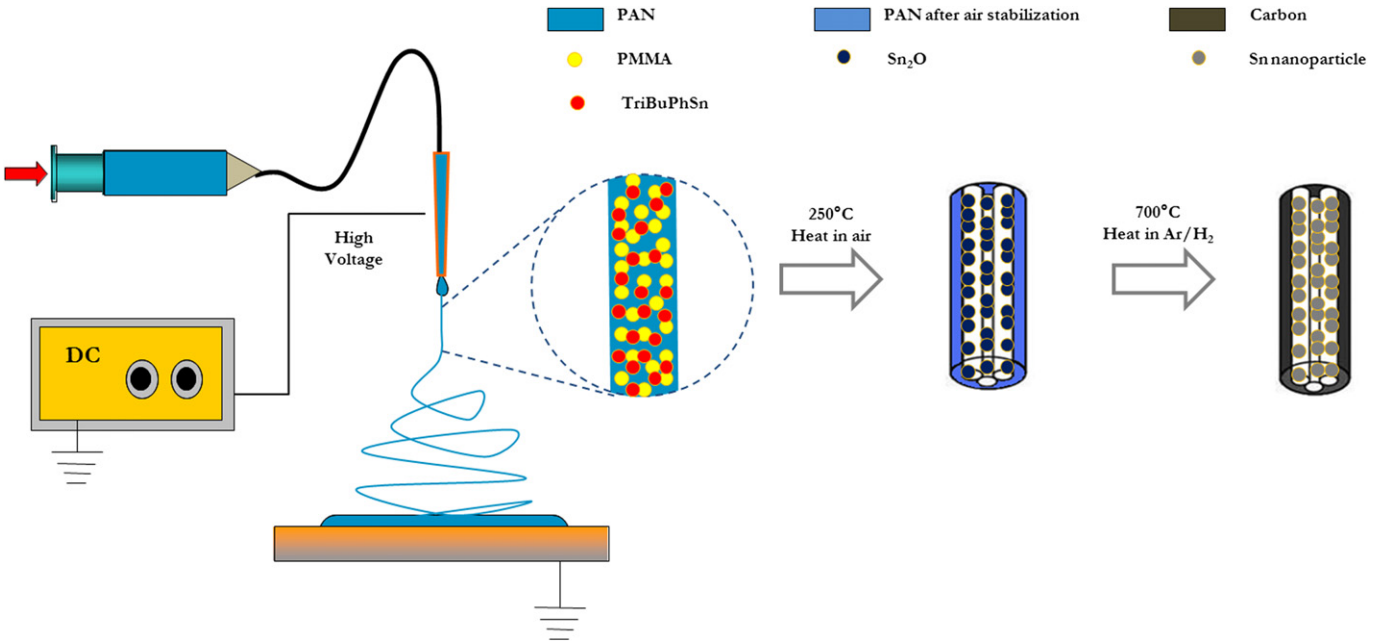

Fig. 1. Schematics of a homemade electrospinning spinneret used in preparing first PAN/PMMA/TBPT nanofibers and Sn@carbon nanoparticles embedded in hollow carbon nanofibers.

H, N, and C contents were determined by direct measurements, while the total Sn + O content was estimated by difference. The crystal structure was investigated by X-ray diffraction using a X'Pert Panalytical Alpha1 diffractometer equipped with a Cu-K_α source (λ = 1.5418 Å). Phase identification and quantification were performed using 'EVA 17.2' and 'TOPAS 4.2' Bruker AXS computer programs, respectively.

The pyrolyzed nanofibrous mats were first manually ground in an agate mortar, then 85 wt.% of the Sn/C composite, 5 wt.% of Super-P (MMM Carbon, Belgium) and 10 wt.% of Na-carboxymethylcellulose (Na-CMC, Aldrich) binder were thoroughly mixed in high-purity deionized water to form homogeneous slurry. This slurry was uniformly spread on a copper foil using the doctor-blade technique to prepare electrode films of 150 μm thickness. After drying at 120 °C in a vacuum oven for 12 h and roll-pressing, disks with a diameter of 9 mm were punched out. The resulting electrodes were 40 μm tick with an active mass loading (Sn/C) of 1.4 mg cm^{-2}.

Electrochemical test cells (Swagelok-type) were assembled in an argon-filled glove box (homemade, H_2O and O_2 content less than 1 ppm) using lithium metal disk as the counter/reference electrodes and 1 M solution of $LiPF_6$ in a 1:1:1 vol/vol/vol mixture of ethylene carbonate (EC), diethyl carbonate (DEC) and dimethyl carbonate (DMC) as electrolyte (LP71, Merck). A glass fiber disk (Whatman) 300 μm thick was used as separator film. The cells were charged and discharged galvanostatically in a voltage range of 5 mV–2 V by using a VMP2/Z Multichannel Galvanostat-Potentiostat (Bio-Logic, France). All the measurements have been performed at T = 20 °C and all potentials are given vs. the $Li^+/Li°$ semi-couple. Where not differently specified, the capacity values refer to specific capacity, calculated with respect to the active mass of the electrodes. The rate-dependent and long-term capacity retention values have been calculated with respect to the capacity obtained during the 110th cycle, performed at 1.9 C rate.

3. Results and discussion

3.1. Chemical, structural and morphological characterization

The synthesis procedure of Sn-PMCMT described in Section 2 and schematized in Fig. 1 determines the peculiar morphology of the composite material inasmuch the Sn nanoparticles are embedded in a carbon matrix. Fig. 2 panels (a), (b) report the SEM images of the as-prepared Sn-PMCMT composite nanofibers. A highly porous carbon mat is formed as a texture of intimately tangled fibers (panel a) having sub micrometer diameters.

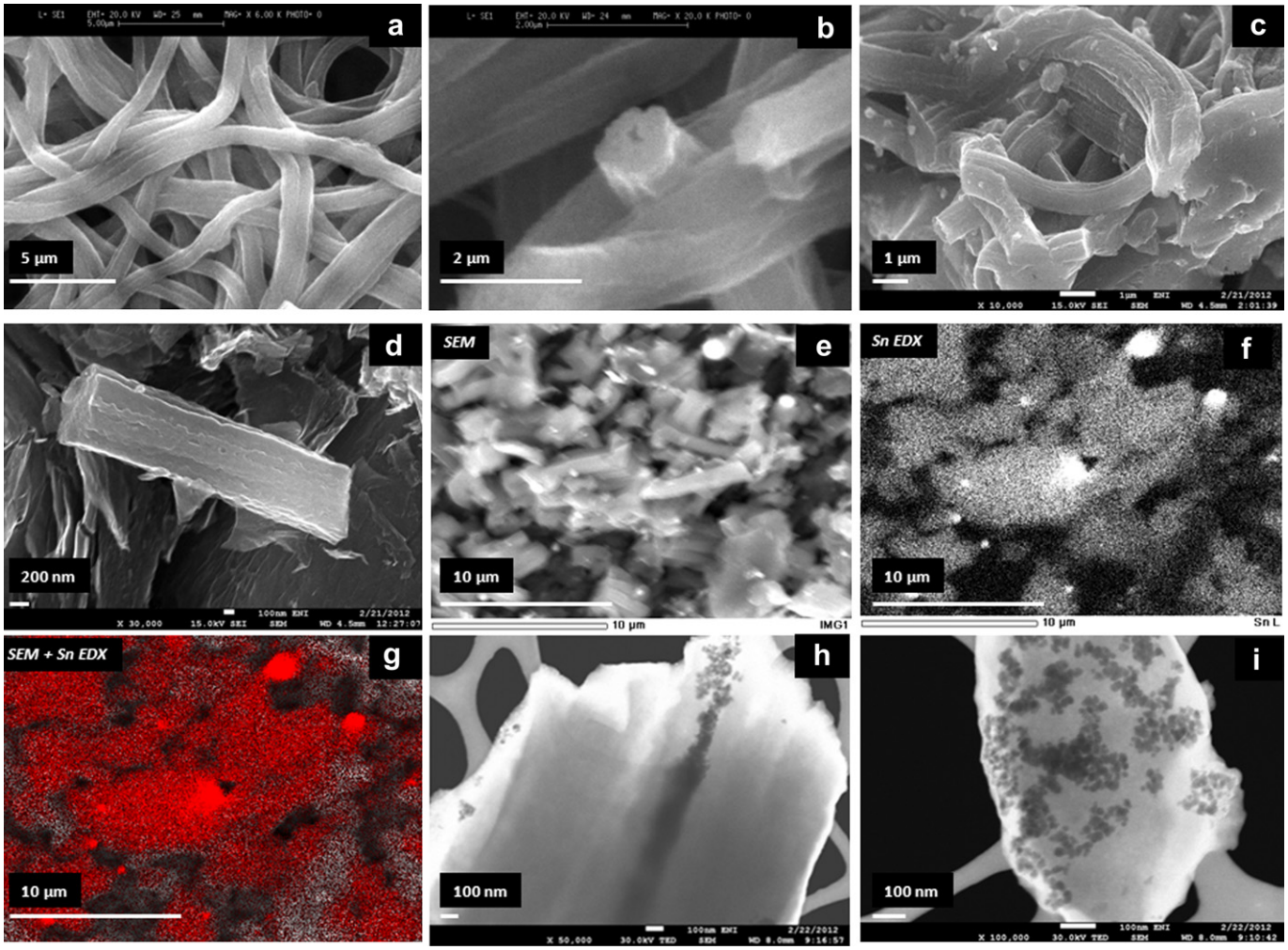

Fig. 2. Secondary electron SEM images at different magnifications of the as-prepared Sn-PMCMT composite nanofibers (a, b). Secondary electron SEM images at different magnifications of the Sn-PMCMT composite nanofibers after grinding (c, d). Secondary electron micrograph (e), EDX mapping of Sn (f), overlapping of Sn EDX mapping to secondary electron micrograph (g) of a portion of the Sn-PMCMT powder. TEM micrograph of Sn-PMCMT fibers (h) and powder (i).

Cross-section details (panel b) reveal that the micro-fibers are, in turn, formed by agglomerations of nanosized fibers separated by hollow channels. Fig. 2 panels (c), (d) highlight the morphology of the powders formed after grinding the carbon mats in a mortar. As a consequence of the treatment the length of the fibers is reduced and a fine powder, mostly formed by nano-cylinders few hundreds nm wide and 1–2 μm long, is formed. A minor fraction of dispersed grains with irregular shapes is also present. Fig. 2 panels (e) and (f) shows the secondary electron micrograph and the Sn EDX mapping, respectively. Panel (g) shows the overlapping of secondary electron micrograph and Sn mapping. The figures clearly reveal that the metallic nanosize tin is finely dispersed throughout the carbon matrix, while a low fraction of the metallic tin appears as micrometer-size aggregates dispersed outside of the PMCMT. Bright-field transmission electron microscopy (TEM) images are shown in Fig. 2 panels (h), (i). The micrographs clearly confirm that most of the Sn is encapsulated as nanosize powder or filaments finely dispersed through the internal hollow channels of the carbon fibers (panel h) or particles (panel i). Only few micrometric particles are located outside of the carbon texture.

This peculiar morphology is expected to be very promising in terms of general electrochemical properties when the composite material is utilized as anode in lithium-ion batteries. In fact, the presence of Sn particles with an average diameter of few tens of nanometers results in a very high surface-to-volume ratio, which is the necessary prerequisite for an electrode operation at very high overall current and possibly enables the realization of high power batteries. In addition, the presence of hollow channels inside the carbon fibers guarantees an easy and fast access of the liquid electrolyte to the tin active material surface. Finally, the confinement of the tin nanoparticles inside the carbon matrix can counteract the volume variations that usually occur during Li–Sn reversible alloying and that is one of the main causes of anode degradation and poor battery cycle life. As an extra benefit, Sn particles appear well embedded inside the carbon matrix, thus determining a protection against tin oxidation by air during the electrode fabrication.

Fig. 3 shows the X-ray diffractogramm (XRD) of the Sn-PMCMT composite material. XRD phase analysis reveals, as main features, peaks that can be indexed to amorphous C (broad background centered at $2\theta \sim 25^\circ$) and metallic Sn (main peaks in the 2θ regions 30°–33° and 44°–46°). The main reflections of metal Sn are indexed according to Miller's notation. Reflections from SnO and SnO_2 are evidenced as well. The occurrence of Sn oxides can be explained by two concurrent mechanisms: (i) the thermal treatment at 700 °C in reducing atmosphere does not allow the complete reduction of SnO_2, which forms by the decomposition of the Sn(IV) organic precursor during the first thermal treatment step at 250 °C in air (see Fig. 1); (ii) part of Sn metallic particles, probably those that are not embedded and protected inside PMCMTs, are oxidized due to the contact with air during the sample handling. The XRD phase analysis yielded an estimated composition $Sn:SnO:SnO_2$ corresponding to 71:16:13 wt.%.

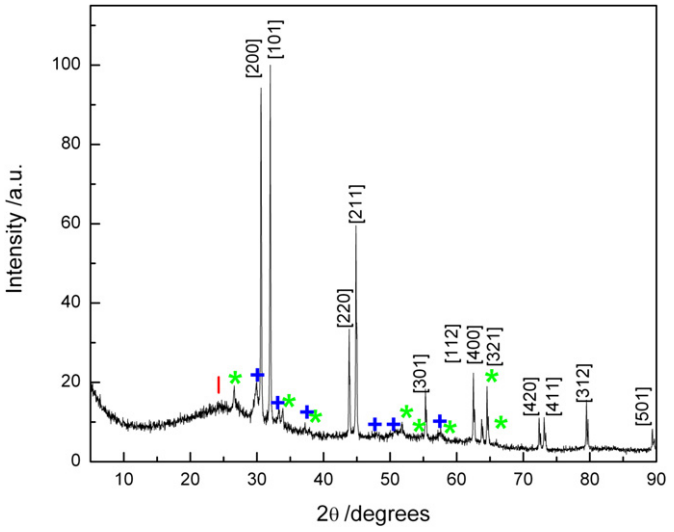

Fig. 3. XRD pattern of Sn-PMCMT composite. The main reflections of metallic Sn are indexed according to Miller's notation. Reflections from carbon, SnO, SnO_2 are marked as (|), (+), (*) respectively. X-ray radiation wavelength $\lambda = 1.5418$ Å (Cu-K_α line).

Elemental analysis reveals that, in addition to the carbon found as main component (C, 55.7 wt.%), nitrogen (N, 9 wt.%) and hydrogen (H, 2 wt.%) are formed as residuals of the thermal treatment of the organic precursors. The presence of N and H can be justified by considering the relatively low temperature (700 °C) utilized during the pyrolysis of the organic matrix [23]. The total fraction of Sn plus O has been calculated by difference and resulted to be 33.3 wt.%. By combining results from elemental analysis and XRD phase analysis, the relative amounts of Sn and O have been estimated as 31.7 and 1.6 wt.%, respectively. Electron microscopy has shown that most of the metallic Sn is contained inside the channels of the carbon fibers as particles of few nanometers and that only a minor fraction is outside the channels, in larger aggregates, not protected by the carbon host fibers against the air oxidation. As a consequence, XRD measurements, that have lower sensitivity toward nanosize powder, may under-estimate the contribution from the metal nanosize particles inside the channels and over-estimate the contribution from larger Sn oxides particles decorating the carbon fibers surface. However, this possible systematic error (that may lead to an uncertainty of only ±1%, or less, in the overall Sn accuracy determination) can be neglected in terms of delivered anodic capacity of the composite material, since after the irreversible reduction of tin oxides to metallic Sn during the first cycle, the whole amount of the formed tin can take part to the subsequent reversible Li–Sn redox processes, regardless of its initial oxidation state.

Details about the elemental and phase compositions are listed in Table 1.

3.2. Electrochemical characterization

To determine the performances of the Sn-PMCMT composite anodes, galvanostatic charge/discharge cycles have been performed at different rates. In order to estimate the theoretical capacity of the electrodes, the composition of the active material, Sn:C/32:66.7 wt.% mass ratio, and the theoretical capacities associated with Li–Sn and Li–C reversible processes should be considered.

Li–Sn alloying occurs as a multi-step electrochemical reduction whose stoichiometry is reported in Eq. (1):

$$4.4Li^+ + 4.4e^- + Sn \rightarrow Li_{4.4}Sn \quad (1)$$

Table 1
Detail of elemental and phase compositions as calculated from combustion elemental analysis and X-ray diffraction phase analysis.

Element	Weight %	Phase	Weight %
Sn	31.7	Sn	23.7
C	55.7	SnO	5.3
H	2.0	SnO_2	4.3
N	9.0	C(H,N-containing)	66.7
O	1.6		

At $T = 25$ °C, the equilibrium potentials for the subsequent alloying steps leading to the $Li_{4.4}Sn$ formation are located in the range 0.8–0.38 V [24]. However, kinetic hindrance usually requires a significant activation energy that leads to electrode polarization and enlarges the potential windows over which the alloying and de-alloying processes take place.

SnO and SnO_2 oxides' impurities present in the Sn-PMCMT composite matrix may contribute to the irreversible capacity during first Li insertion step, due to the formation of an additional amount of metallic Sn and Li_2O at potentials higher than 1 V. The formation of Li_2O is irreversible and the lithium consumed in the reaction represents an irreversible capacity loss. Nonetheless, this process could be beneficial to the overall electrode performances as it leads to a composite microstructure containing Li_2O, a Li^+ conducting solid electrolyte that could improve the kinetics of the alloying/de-alloying processes. In conclusion, after the first reduction cycle all the Sn present in the composite, regardless of its initial chemical status, shall contribute to the overall electrode reversible capacity of 994 mAh g^{-1} due to the formation $Li_{4.4}Sn$. At the same time, the amorphous C matrix of the Sn-PMCMT composite dictates the nature and the extent of both irreversible and reversible Li–C storage processes. Morphological and chemical features, such as the surface-to-volume ratio, the presence of defects, pores, cavities, and the introduction of C–H and C–N functionalities [25,26] usually determine the extent of solid electrolyte interphase (SEI) formation at about 0.8 V, the shape of E vs. Q profiles and the capacity and reversibility of the charge/discharge processes. In fact, extra Li-storage processes in pores, cavities and vacancies of amorphous carbons take place over the 0–1 V range without any evident plateaus.

In the present case, the carbon forming the PMCMTs, due to the maximum (700 °C) temperature of synthesis adopted, is expected to be a hydrogen-containing soft carbon. This kind of carbon, often reported as 'Low-T carbon', is known to give rise to large initial capacity loss, with a pronounced hysteresis between reduction and oxidation [23,26,27]. Literature reports that Low-T carbons are capable to supply Li-storage capacities between 400 and 2000 mAh g^{-1} associated with poor cycling performance [28]. In addition most of the Li^+ storage in Low-T carbon occurs close to 0 V and the capacity may be severely limited by the cell polarization that depends on the actual cycling rate.

Summarizing, it is difficult to rigorously predict the C contribution to Li^+ storage, and hence the overall value of the electrode reversible capacity. As a consequence, the 'benchmark' Sn/C electrode capacity has been assumed in the range 400–500 mAh g^{-1}, as reported in several papers dealing with Sn/C nanocomposite electrodes [18,19,29–31], while the unitary 1 C cycling rate has been taken as 500 mA g^{-1}, a value that is in agreement with the one proposed by Yu et al. [18,19] for galvanostatic cyclations on Sn/C composites with similar morphology.

Fig. 4 displays the voltage profiles at different charge/discharge rates of some relevant cycles performed on electrochemical cells using Sn-PMCMT composite anode. Cycles 1 and 2 have been performed at the relatively low rate of 0.2 C (100 mA g^{-1}) in order to allow full and homogeneous SEI formation and complete tin oxides reduction. The profile related to the first Li^+ insertion corresponds to an initial capacity of about 1400 mAh g^{-1}. This very large value is a consequence of the carbon morphology that, because of the porous multichannel structure, has a very high specific surface area. The subsequent charge/discharge processes at 0.2 C rate (first de-alloying and second cycle) yield reversible capacity values of about 800 mAh g^{-1}. These values are quite higher than the estimated values of about 400–500 mAh g^{-1} and can be justified by considering that different Sn/C nanocomposites may exhibit different C morphologies and, as a consequence, may be involved in different Li–C surface storage processes.

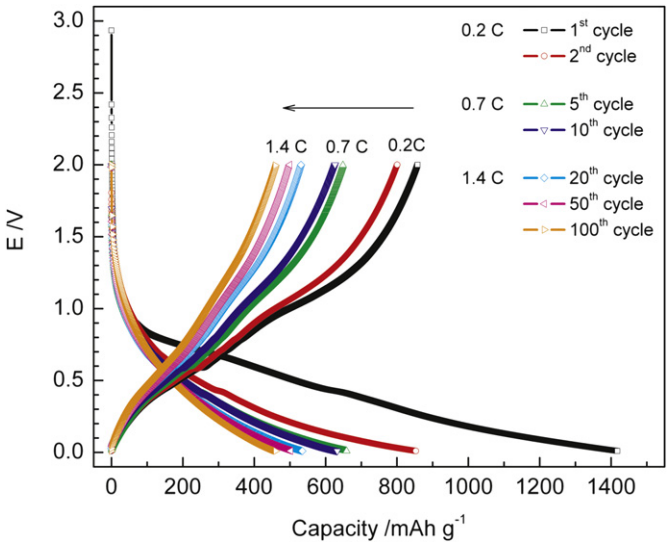

Fig. 4. Galvanostatic E vs. Q profiles of selected cycles between the 1st and the 100th cycles. Charge/discharge rates: 0.2 C (cycles 1, 2), 0.7 C (cycles 5, 10), 1.4 C (cycles 20, 50, 100), 0.01 V < E < 2 V, $T = 20$ °C.

The characteristic Li–Sn alloying/de-alloying reactions are shown as shoulders between 0.4 V and 0.8 V. These features are superimposed over monotonous profiles related to Li–C reversible storage processes, which are characterized by a large charge/discharge potential hysteresis. The large shoulders at potentials above 1 V, clearly visible in de-alloying profiles, may be assigned to a kinetically hindered release of Li^+ stored at carbon surface and cavities [26]. When the charge/discharge rate is increased up to 0.7 C (5th and 10th cycles) and 1.4 C (20th, 50th, 100th cycles), the carbon contribution to Li^+ storage is affected by an increasing ohmic polarization, so that the capacity values level to about 600 mAh g^{-1} and 450 mAh g^{-1}, respectively.

Fig. 5 shows the values of capacity delivered by the composite anode during the first 100 cycles performed at current rates 0.2 C (cycles 1–3), 0.7 C (cycles 4–13), 1.4 C (14–100), and the related coulombic efficiencies. During the initial cycles a rapid capacity fade occurs, due to some irreversible Li^+ storage processes.

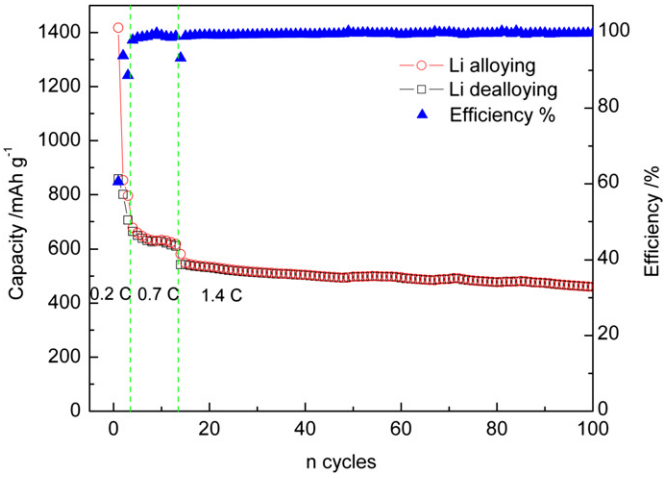

Fig. 5. Capacity and efficiency of the Sn/C composite electrode during the first 100 cycles. Charge/discharge rates 0.2 C (cycles 1–3), 0.7 C (cycles 4–13), 1.4 C (cycles 14–100), 0.01 V < E < 2 V, $T = 20$ °C.

However, irreversible capacity at first cycle is about 40%, which is a higher value compared to standard graphite anodes, but still relatively low when Li–Sn alloy anodes are taken into account [30].

During the following cycles, at each charge/discharge rate the capacity tends to steady values that comprise both contributions from Li–Sn alloying and Li–C storage. The capacity and coulombic efficiency of selected cycles are reported in Table 2. A more accurate characterization of the Li–Sn and Li–C processes can be done by analyzing the $dQ\ dE^{-1}$ vs. E differential profiles, reported in Fig. 6. Two features related to irreversible processes are clearly visible during the first reduction. At about 1 V a minor peak, marked as (a), may be assigned to the reduction of Sn oxides to metallic Sn [10]. This confirms that only minor amounts of SnO_2 are formed during the Sn-PMCMT synthesis (and that the XRD phase analysis may over-estimate the content of Sn oxides at the surface of carbon micro-fibers). In addition, the absence of a peak at about 1.5 V confirms that metallic Sn is well dispersed and encapsulated [29] inside hollow channels of carbon fibers. In fact, a nanosize Sn powder directly exposed to electrolyte would otherwise catalyze the electrolyte decomposition at about 1.5 V [32,33]. A broad peak (b) related to SEI formation at carbon fibers surface, is centered at about 0.75 V and extends at lower voltages because of kinetic issues.

The main features related to reversible processes are evidenced in the voltage range 0.4–0.8 V. Two small cathodic peaks at about 0.67 V (c) and 0.55 V (d) and a sharp peak at 0.43 V (e) are the signature of Li–Sn alloying processes [29] taking place during the electrode reduction. On the anodic side, peaks related to Li–Sn de-alloying are clearly visible at 0.45 V (f), 0.59 V (g), 0.72 V (h) and 0.79 V (i). The shift between charge and discharge potentials is typical of Li–Sn alloy electrodes [29,30] and may be ascribed to different reaction mechanisms and kinetics of the forward and backward processes, which respectively lead to formation of $Li_{4.4}Sn$ and Sn as end-terms. It is worth noting that, at least at 0.2 C cycling rate, the Li–Sn peaks are retained during the following cycles, suggesting a quite stable morphology for the metallic Sn particles embedded in the carbon micro-fibers.

The profiles of cycles 5 and 10, performed at a higher current rate (0.7 C), still reveal Li–Sn reversible peaks with reduced areas. When the rate is raised up to 1.4 C and the number of cycles is increased up to 20, 50, 100, the sharp Li–Sn peaks progressively disappear, probably because of kinetic issues that lead to coexistence of several phases in a broad potential window.

The main Li–C reversible processes are evidenced during electrode reduction. A continuous baseline, related to reversible reaction of C surface and edge sites with Li^+, extends down to the low cut-off potential of 0.01 V. A cathodic shoulder between 0.3 and 0.01 V, marked as (j), is the signature of Li insertion between disordered graphene planes of the carbon matrix. The coupled inverse oxidation processes, related to the extraction of Li^+ from carbon structure and surface, are evidenced by a broad anodic peak at about 1 V, marked as (k). The large hysteresis between anodic and cathodic processes, which is typical of H-containing, low-T carbons [26], is consistent with the charge/discharge behavior of Sn/C composites with similar morphology [19]. The anodic peak becomes less pronounced and shifts to higher potentials upon cycling, probably because of a progressive worsening of kinetics [23–27].

The rate capability of the anode has been evaluated at progressively higher rates for additional 100 cycles up to 10 C. Fig. 7 clearly shows that the electrode is still able to deliver relatively high capacities at increased current rates. Values for capacity and capacity retention of selected cycles are listed in Table 3. Worth to be noticed is that at 3.2 C and 5.1 C rates, corresponding to specific

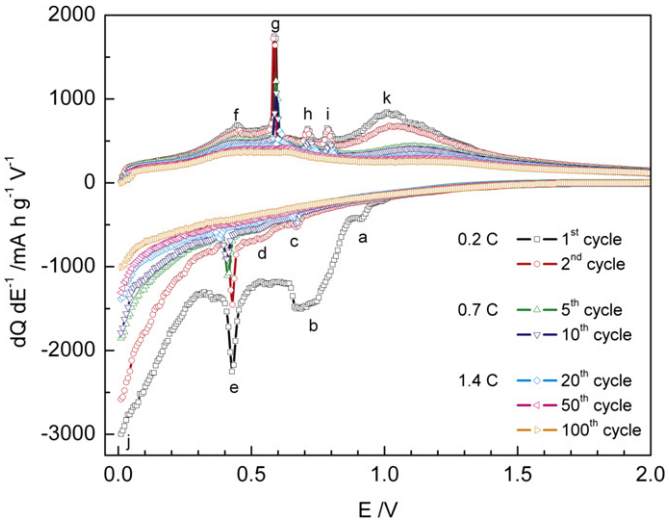

Fig. 6. Differential $dQ\ dE^{-1}$ vs. E profiles of selected cycles between the 1st and the 100th cycles. Peaks related to irreversible processes Sn oxides reduction, SEI formation, reversible Li–Sn processes and reversible Li–C processes are marked as (a), (b), (c–i), (j, k) respectively. Charge/discharge rates 0.2 C (cycles 1, 2), 0.7 C (cycles 5, 10), 1.4 C (cycles 20, 50, 100), 0.01 V < E < 2 V, T = 20 °C.

Table 2
Values of capacity and efficiency obtained at selected cycles between the 1st and the 100th cycles. Charge/discharge rates 0.2 C (cycles 1–3), 0.7 C (cycles 4–13), 1.4 C (cycles 14–100). 0.01 V < E < 2 V, T = 20 °C.

Cycle	C rate	Capacity/mAh g^{-1}		Efficiency/%
		Li alloying	Li de-alloying	
1	0.2 C	1417.5	858.2	60.5
2	0.2 C	853.2	800.8	93.9
3	0.2 C/0.7 C[a]	795.7	705.5	88.7
5	0.7 C	658.4	649.1	98.6
10	0.7 C	632.1	627.4	99.3
13	0.7 C	617.3	611.1	99.0
20	1.4 C	534.7	531.4	99.43
30	1.4 C	515.3	512.3	99.4
50	1.4 C	497.8	497.1	99.9
100	1.4 C	460.4	459.8	99.9

[a] Alloying performed at 0.2 C rate, de-alloying at 0.7 C rate.

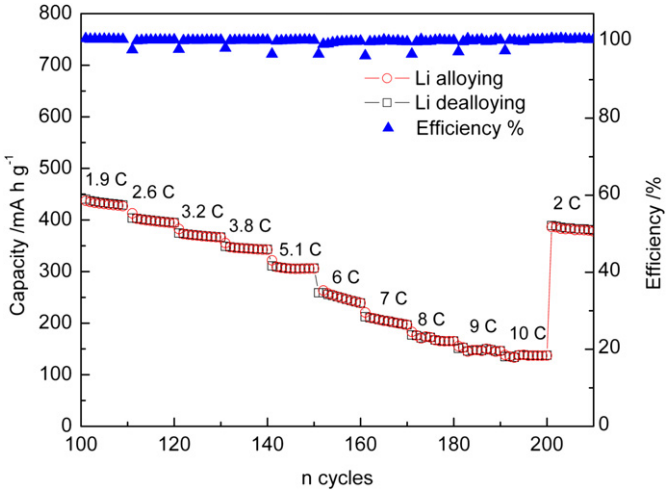

Fig. 7. Capacity and efficiency of the Sn/C composite electrode as a function of cycling rate between 100th and 210th cycles. Charge/discharge rates between 1.9 C and 10 C, 0.01 V < E < 2 V, T = 20 °C.

Table 3
Values of rate-dependent and long-term capacity and capacity retention obtained at selected cycles between the 110th and the 600th cycles. The capacity retention is calculated with respect to the reference value obtained during 110th cycle, performed at rate 1.9 C. Charge/discharge rates between 1.9 C and 10 C. The corresponding specific current and current density values are shown. 0.01 V < E < 2 V, T = 20 °C.

Cycle	110	120	130	140	150	160	170	180	190	200	210	280	400	600
C rate	1.9 C	2.8 C	3.2 C	3.8 C	5.1 C	6 C	7 C	8 C	9 C	10 C	2 C	2 C	2 C	2 C
Specific current/A g^{-1}	0.95	1.3	1.6	1.9	2.55	3	3.5	4	4.5	5	1	1	1	1
Current density/mA cm^{-2}	1.1	1.6	1.9	2.3	3.1	3.6	4.2	4.8	5.4	6.1	1.2	1.2	1.2	1.2
Capacity/mAh g^{-1}	429[a]	395	367	343	307	239	197	165	146	138	380	332	339	337
Capacity retention/%	100	92	86	80	72	56	46	39	34	32	89	78	79	79

[a] Reference value for calculation of capacity retention.

currents of 1.6 A g^{-1} and 2.55 A g^{-1} and current densities of 1.9 A cm^{-2} and 3.1 A cm^{-2}, the electrode exhibits 86% and 72% capacity retention, respectively. Even at the very high rates of 8 C and 10 C, corresponding to 4 A g^{-1} and 5 A g^{-1} and 4.8 mA cm^{-2} and 6.1 mA cm^{-2}, the capacity retention of the electrode is 39% and 32%, i.e. 165 mAh g^{-1} and 138 mAh g^{-1}, respectively. These characteristics outperform similar Sn/C composites reported in the literature, which are commonly cycled at rates not exceeding 5 C (i.e. 2.5 A g^{-1}, based on a value of 1 C estimated as 500 mA g^{-1}) [29–31].

All the charge/discharge cycles take place with coulombic efficiency close to unity (99.9% or higher). In addition, when the charge/discharge rate is restored to 2 C, a rate close to the initial reference conditions, 89% of capacity is still retained.

The long-term cycling stability of the Sn-PMCMT composite electrodes has been evaluated by extending the galvanostatic cycling by 400 additional cycles at 2 C charge/discharge rate (Fig. 8). The specific capacity and capacity retention of selected cycles are reported in Table 3. After an initial decay, the capacity stabilizes at values around 340 mAh g^{-1}, even if there are oscillations probably caused by fluctuations in the temperature during the long-term experiments. At the 600th cycle, the capacity is still 337 mAh g^{-1}, which corresponds to a capacity retention of about 79%. Also in these conditions, all the charge/discharge cycles show a coulombic efficiency close to unity.

The outstanding performance of the Sn-PMCMT composite electrode is probably rooted in its peculiar morphology. In fact, the nanometric size of the Sn particles and their fine dispersion through the hollow C fibers concur to efficiently buffer the large volume changes usually taking place during Li–Sn alloying/de-alloying processes. Moreover, the nanosize tin particles reduce the transport length for both lithium ions and electrons. Finally, for the sake of comparison, it should be noted that this outstanding long-term cycle life has been here evaluated for 400 consecutive cycles in very demanding conditions for the anode, i.e. adopting a charge/discharge rate (2 C = 1000 mA g^{-1}) that is much higher than the ones (roughly between 0.1 C and 0.8 C) commonly used in the literature to estimate the cycle life of analogous C-encapsulated Sn anodes [28,30,33].

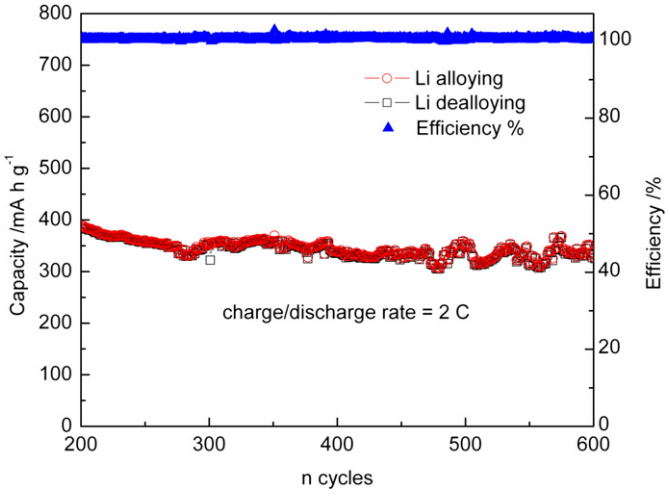

Fig. 8. Long-term capacity and efficiency of the Sn/C composite electrode cycled at 2 C rate between the 200th and the 600th cycles, 0.01 V < E < 2 V, T = 20 °C.

4. Conclusions

A nanostructured Sn-PMCMT composite, in which nanosize Sn is encapsulated inside hollow channels of carbon micro-fibers, has been synthesized by co-electrospinning and successfully applied as an anode material for Li-ion batteries. The introduction of a Na-CMC binder in the anode formulation allowed a greener, safer and cheaper organic-solvent-free procedure for electrode preparation.

The composite anode has shown outstanding electrochemical performance in terms of reversible capacity (and of a relatively low irreversible capacity), rate capability and cycle life, which have been evaluated in very demanding charge/discharge conditions.

This outstanding behavior is probably due to a quite stable encapsulation of the nanoscale metal particles inside hollow carbon fibers, as suggested by the reproducibility of the voltage profiles upon cycling. In fact, this peculiar morphology is able both to prevent potentially hazardous Sn/electrolyte decomposition reactions and to efficiently buffer the dramatic volume changes associated with Li–Sn reversible alloying processes.

These overall features make the here proposed composite material an ideal candidate for the development of safe, high-energy-density, long-cycle-life anodes for Li-ion batteries.

Acknowledgments

The researches leading to these results have received funding from the European Union Seventh Framework Programme (FP7/2007-2013) under grant agreement n° 265644, Project “APPLES Advanced, High Performance, Polymer Lithium Batteries for Electrochemical Storage”. The authors deeply thank Dr. Laura Meda and Dr. Gianluigi Marra for the SEM/TEM and EDX measurements and analysis.

References

[1] J.-M. Tarascon, Philos. Trans. R. Soc. A 368 (2010) 3227.
[2] F. Croce, M.L. Focarete, J. Hassoun, I. Meschini, B. Scrosati, Energy Environ. Sci. 4 (2011) 921.
[3] Y. Idota, T. Kubota, A. Matsufuji, Y. Maekawa, T. Miyasaka, Science 276 (1997) 1395.
[4] J.M. Tarascon, P. Poizot, S. Laruelle, S. Grugeon, L. Dupont, Nature 407 (2000) 496.
[5] A.S. Aricò, P. Bruce, B. Scrosati, J.M. Tarascon, W. van Schalkwijk, Nat. Mater. 4 (2005) 366.
[6] J. Maier, Nat. Mater. 4 (2005) 805.

[7] J. Chen, L. Xu, W. Li, X. Gou, Adv. Mater. 17 (2005) 582.
[8] X.W. Lou, Y. Wang, C. Yuan, J.Y. Lee, L.A. Archer, Adv. Mater. 18 (2006) 2325.
[9] M. Winter, G.H. Wrodnigg, J.O. Besenhard, W. Biberacher, P. Novak, J. Electrochem. Soc. 147 (2000) 2427.
[10] I.A. Courtney, J.R. Dahn, J. Electrochem. Soc. 144 (1997) 2045.
[11] M. Winter, J.O. Besenhard, Electrochim. Acta 45 (1999) 31.
[12] S. Grugeon, S. Laruelle, R. Herrera-Urbina, L. Dupont, P. Poizot, J.M. Tarascon, J. Electrochem. Soc. 148 (2001) A285.
[13] E. Shembel, R. Apostolova, V. Nagirny, I. Kirsanova, Ph. Grebenkin, P. Lytvyn, J. Solid State Electrochem. 9 (2005) 96.
[14] K.T. Lee, Y.S. Jung, S.M. Oh, J. Am. Chem. Soc. 125 (2003) 5652.
[15] H.S. Choi, J.G. Lee, H.Y. Lee, S.W. Kim, C.R. Park, Electrochim. Acta 56 (2010) 790.
[16] Y. Yu, Q. Yang, D. Teng, X. Yang, S. Ryu, Electrochem. Commun. 12 (2010) 1187.
[17] E. Zussman, A.L. Yarin, A.V. Bazilevsky, R. Avrahami, M. Feldman, Adv. Mater. 18 (2006) 348.
[18] Y. Yu, L. Gu, C. Zhu, P.A. van Aken, J. Maier, J. Am. Chem. Soc. 131 (2009) 15984.
[19] Y. Yu, L. Gu, C. Wang, A. Dhanabalan, P.A. van Aken, J. Maier, Angew. Chem. Int. Ed. 48 (2009) 6485.
[20] J. Li, R.B. Lewis, J.R. Dahn, Electrochem. Solid State Lett. 10 (2007) A17.
[21] B. Lestriez, S. Bahri, I. Sandu, L. Roué, D. Guyomard, Electrochem. Commun. 9 (2007) 2801.
[22] K.T. Lee, Y.S. Jung, S.M. Oh, J. Am. Chem. Soc. 125 (2003) 5653.
[23] J.R. Dahn, T. Zheng, Y. Liu, J.S. Xue, Science 270 (1995) 590.
[24] R.A. Huggins, J. Power Sources 81–82 (1999) 13.
[25] N.A. Kaskhedikar, J. Maier, Adv. Mater. 21 (2009) 2664.
[26] T. Zheng, W.R. McKinnon, J.R. Dahn, J. Electrochem. Soc. 143 (1996) 2137.
[27] M. Winter, K.-C. Moeller, J.O. Besenhard, in: G.-A. Nazri, G. Pistoia (Eds.), Lithium Batteries. Science and Technology, Kluwer, New York, 2004, p. 160.
[28] M. Winter, J.O. Besenhard, M.E. Spahr, P. Novak, Adv. Mater. 10 (1998) 725.
[29] Y.S. Jung, K.T. Lee, J.H. Ryu, D. Im, S.M. Oh, J. Electrochem. Soc. 152 (2007) A1452.
[30] J. Hassoun, G. Derrien, S. Panero, B. Scrosati, Adv. Mater. 20 (2008) 3169.
[31] G. Derrien, J. Hassoun, S. Panero, B. Scrosati, Adv. Mater. 19 (2007) 2336.
[32] L.Y. Beaulieu, S.D. Beattie, T.D. Hatchard, J.R. Dahn, J. Electrochem. Soc. 150 (2003) A419.
[33] N. Pereira, L.C. Klein, G.G. Amatucci, Solid State Ionics 167 (2004) 29.